JACS
JOURNAL OF THE AMERICAN CHEMICAL SOCIETY
pubs.acs.org/JACS
Article

Lutetium Texaphyrin–Celecoxib Conjugate as a Potential Immuno-Photodynamic Therapy Agent

Jusung An,[#] Kong-Peng Lv,[#] Calvin V. Chau,[#] Jong Hyeon Lim,[#] Rakesh Parida, Xin Huang, Snehasish Debnath, Yunjie Xu, Siqi Zheng, Adam C. Sedgwick, Jin Yong Lee,[*] Dixian Luo,[*] Quan Liu,[*] Jonathan L. Sessler,[*] and Jong Seung Kim[*]

Cite This: https://doi.org/10.1021/jacs.4c05978
Read Online

ABSTRACT: Immuno-photodynamic therapy (IPDT) has emerged as a new modality for cancer treatment. Novel photosensitizers can help achieve the promise inherent in IPDT, namely, the complete eradication of a tumor without recurrence. We report here a small molecule photosensitizer conjugate, LuCXB. This IPDT agent integrates a celecoxib (cyclooxygenase-2 inhibitor) moiety with a near-infrared absorbing lutetium texaphyrin photocatalytic core. In aqueous environments, the two components of LuCXB are self-associated through inferred donor–acceptor interactions. A consequence of this intramolecular association is that upon photoirradiation with 730 nm light, LuCXB produces superoxide radicals ($O_2^{-\bullet}$) via a type I photodynamic pathway; this provides a first line of defense against the tumor while promoting IPDT. For in vivo therapeutic applications, we prepared a CD133-targeting, aptamer-functionalized exosome-based nanophotosensitizer (Ex-apt@LuCXB) designed to target cancer stem cells. Ex-apt@LuCXB was found to display good photosensitivity, acceptable biocompatibility, and robust tumor targetability. Under conditions of photoirradiation, Ex-apt@LuCXB acts to amplify IPDT while exerting a significant antitumor effect in both liver and breast cancer mouse models. The observed therapeutic effects are attributed to a synergistic mechanism that combines antiangiogenesis and photoinduced cancer immunotherapy.

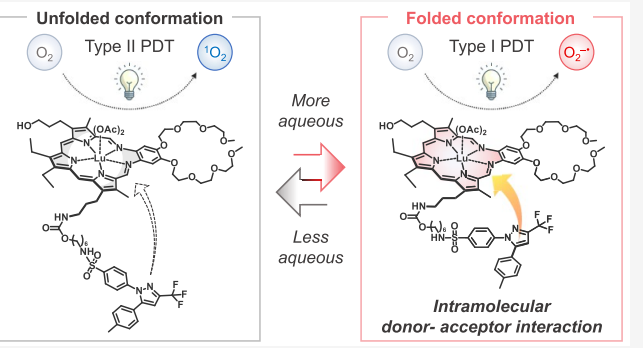

INTRODUCTION

Photodynamic therapy (PDT), which relies on a combination of photosensitizers and light, is an established modality that has been used to treat a range of cancerous diseases. In favorable scenarios, it benefits from several advantages, including low systemic toxicity, minimal invasiveness, and light-based spatiotemporal control.[1] However, traditional PDT is subject to limitations, including a need to achieve effective through-tissue light penetration and reliance on endogenous oxygen to mediate its cytotoxic effects. Moreover, PDT often fails to achieve comprehensive tumor eradication or prevent cancer recurrence and metastasis.[2] To address these latter limitations, an effort is being made to develop PDT modalities integrated with immunotherapy. This approach referred to as immuno-photodynamic therapy (IPDT), is designed to boost the immune system by triggering so-called immunogenic cell death.[3,4] Briefly, upon exposure to light irradiation, IPDT photosensitizers catalyze the conversion of oxygen molecules into cytotoxic reactive oxygen species (ROS), thereby initiating cell death processes (e.g., apoptosis, pyroptosis, and necroptosis).[2] The resulting demise of tumor cells triggers the release of damage-associated molecular patterns, tumor-specific antigens, and proinflammatory cytokines, exposes additional immunogens, and activates the immune system within the tumor microenvironment.[2,5] IPDT can thus promote the transition of immune-off to immune-on tumors while triggering a systemic immune response that ideally prevents cancer recurrence (via, e.g., enhanced tumor infiltration of immune cells and an amplified antitumor immune response against solid tumors).[6] These perceived benefits make IPDT attractive as a tumor control strategy.[7]

Given the critical role of photosensitizers in PDT, considerable ongoing effort is being devoted to improving their efficacy.[3] For example, key goals are to create systems that (1) function in hypoxic tumor environments,[8−10] (2) absorb strongly in the near-infrared (NIR) spectral region and allow for deep tissue light penetration,[11,12] (3) operate via

Received: May 1, 2024
Revised: June 14, 2024
Accepted: June 18, 2024

Scheme 1. Previously Reported Small Molecule Photosensitizer Conjugates (SMPCs) Designed to Produce a Synergistic Photodynamic Therapy (PDT) Effect and the Present SMPC-Based Approach to Immuno-Photodynamic Therapy (IPDT); as Detailed in the Text, It Relies on Convertible Reactive Oxygen Species (ROS) Generation to Boost the Tumor Immune Response and Promote Antiangiogenesis. PS = Photosensitizer

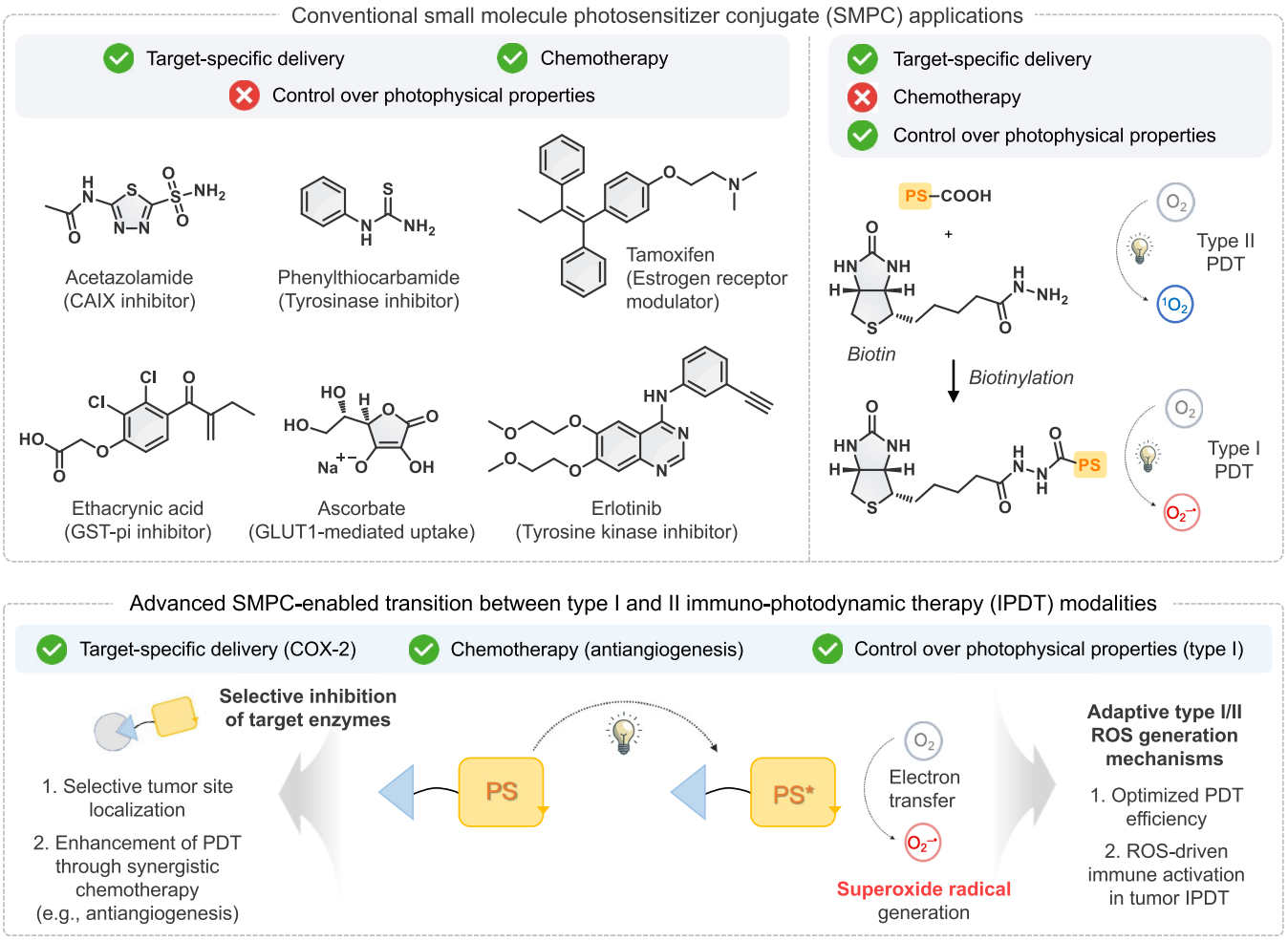

nontraditional photosensitizing mechanisms (e.g., photoredox catalysis),[13,14] (4) display minimal dark toxicity and high biocompatibility,[15−17] and (5) exploit additional therapeutic mechanisms to synergize the effects of PDT.[18,19] One promising approach involves the creation of so-called small molecule photosensitizer conjugates (SMPCs) where a photosensitizer is linked to one or more ancillary species. These latter can consist of cancer-targeting moieties, elements designed to elicit synergistic antitumor effects or mitigate off-target cytotoxicity for normal tissues.[20] In our previous SMPC-related studies, a BODIPY photosensitizer was combined with an acetazolamide moiety to inhibit carbonic anhydrase IX, and thus block angiogenic signaling to overcome the limits of PDT in tumoral hypoxic environments.[21] Subsequently, Kim and Peng reported a system that relies on tamoxifen, an inhibitor of intracellular O_2 consumption and a disrupter of mitochondrial energy metabolism, to achieve O_2-independent PDT.[22] More recently, a Trojan Horse-like cancer-targeting strategy was developed that exploits an ascorbate unit to target glucose transporter 1 to disrupt redox homeostasis.[23] In separate work, An et al. prepared biotin-conjugated photosensitizers that are capable of generating superoxide radical ($O_2^{-\bullet}$) via a type I photodynamic mechanism (Schemes 1 and S1).[24]

Many solid tumor microenvironments are characterized by hypoxia (pO_2 < 5 mmHg), which imparts resistance to oxygen-dependent phototherapies, including IPDT.[25] Recognizing this, we sought to develop an IPDT sensitizer that would promote immunoactivity via $O_2^{-\bullet}$ production even in relatively low oxygen environments, such as those associated with hypoxia. Here, we report the preparation of texaphyrin−celecoxib conjugates and show that they allow effective cancer-targeting and angiogenic signal inhibition while promoting a photoinduced immunogenic response (Scheme 1).

Texaphyrins are aqueous-soluble tripyrrolic penta-aza Schiff base aromatic expanded porphyrins that exhibit strong low-energy absorption bands in the 700−780 nm spectral range[26,27] and form stable 1:1 complexes with a variety of relatively large metal cations. A representative diamagnetic lutetium(III) texaphyrin (LuTex), known as motexafin lutetium, was studied early on as a PDT photosensitizer by researchers at Pharmacyclics Inc.[28] Due to its peripheral water-solubilizing groups, LuTex is an amphipathic molecule that localizes effectively in cancerous lesions. LuTex has a long-lived triplet state and, upon photoirradiation, produces singlet oxygen ($^1O_2$) in high quantum yield via a type II photo-

https://doi.org/10.1021/jacs.4c05978
J. Am. Chem. Soc. XXXX, XXX, XXX−XXX

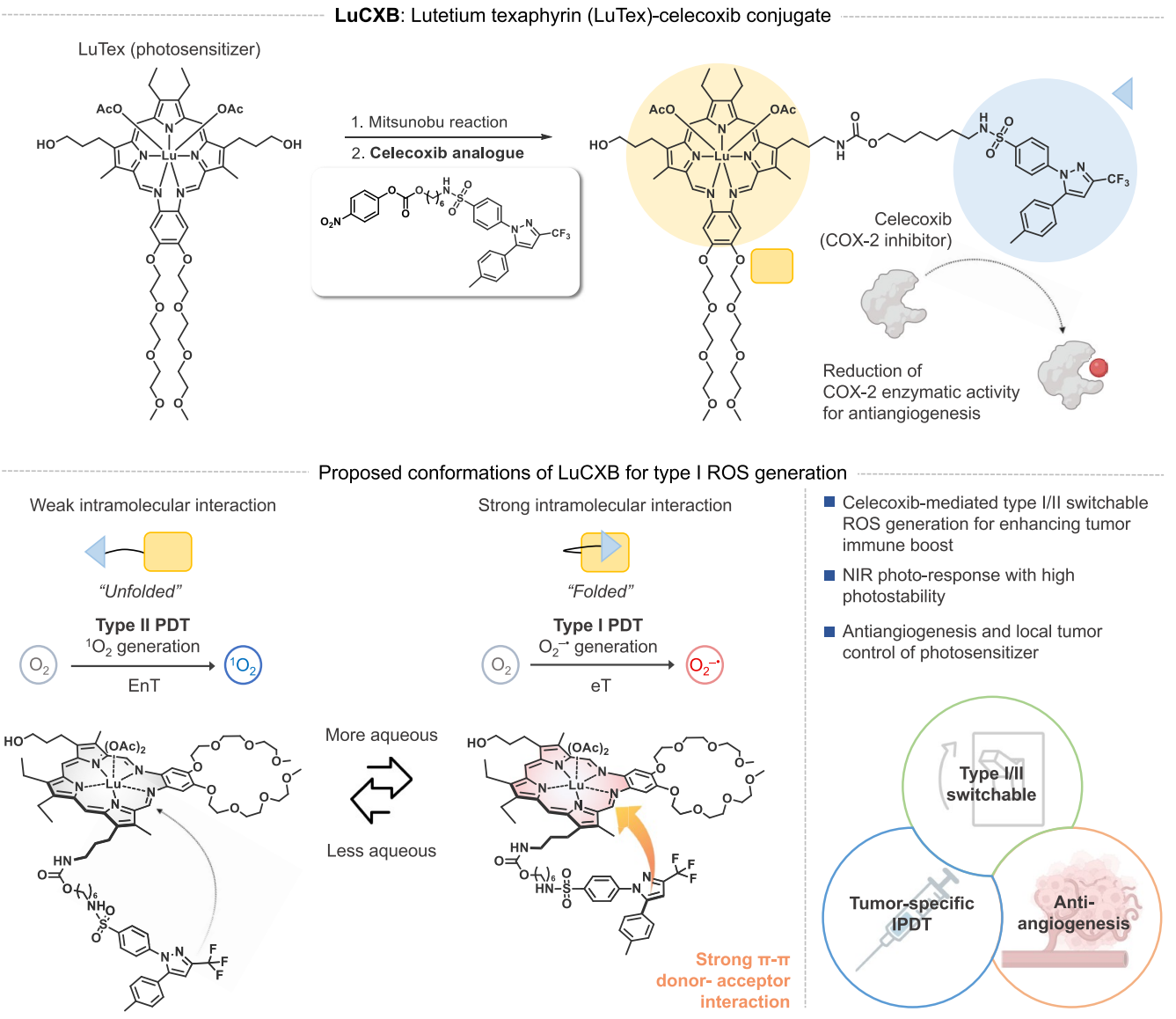

Figure 1. Chemical structures and abbreviated synthetic route to the lutetium texaphyrin (LuTex)-derived, celecoxib-containing SMPC of this study (LuCXB). Schematic illustration showing the conversion between dominant type II and type I ROS generation as a function of the medium. Also shown are the proposed synergistic antiangiogenetic effects and tumor immune boost expected in cancer stem cells. Abbreviations: COX-2, cyclooxygenase-2; EnT, energy transfer; eT, electron transfer; ROS, reactive oxygen species; NIR, near-infrared.

dynamic mechanism.[29] It was found to be an effective photosensitizer in mammary carcinoma mouse models.[30]

Celecoxib is a nonsteroidal anti-inflammatory drug that is used clinically as a cyclooxygenase-2 (COX-2) inhibitor.[31] COX-2 catalyzes the conversion of arachidonic acid to prostaglandin E2 (PGE2). It is overexpressed on tumor membranes, including in breast, lung, colorectal, pancreatic, and liver cancers. This makes it an appealing target for creating drug delivery systems.[32,33] Moreover, PGE2 is a tumor-derived angiogenic factor that is linked to vascular endothelial growth factor (VEGF)-independent angiogenesis.[31] COX-2 inhibition is believed to enhance the blockade of the VEGF pathway, suppress angiogenesis, prevent tumor growth and metastasis, and thus increase overall survival rates.[32,34,35]

Recognizing the complementary features of LuTex and celecoxib, we designed and synthesized an SMPC combining both elements (LuCXB; Figure 1). The underlying design rationale was that the celecoxib moiety would provide local tumor control and inhibit angiogenesis of the tumor vasculature within the tumor microenvironment, while the LuTex core would allow for tumor targeting and act as a photosensitizer. In aqueous media, $\pi-\pi$ donor–acceptor interactions between the celecoxib units and the LuTex core predominate. The photophysical properties of LuCXB are thus controlled such that $O_2^{-\bullet}$ is generated under conditions of photoirradiation. A transition in the ROS-generation mechanisms from type II to I is thus seen. The potential utility of LuCXB in therapeutic applications is supported by in vivo studies involving a nanodrug delivery platform (i.e., a cancer stem cell-targeting CD133 aptamer-decorated exosome)[36−40] as detailed below.

RESULTS AND DISCUSSION

Design, Synthesis, and Photoactivity of LuCXB. The LuTex–celecoxib SMPC (LuCXB) of this study was synthesized as shown in Schemes S2–S4 in the Supporting

https://doi.org/10.1021/jacs.4c05978
J. Am. Chem. Soc. XXXX, XXX, XXX−XXX

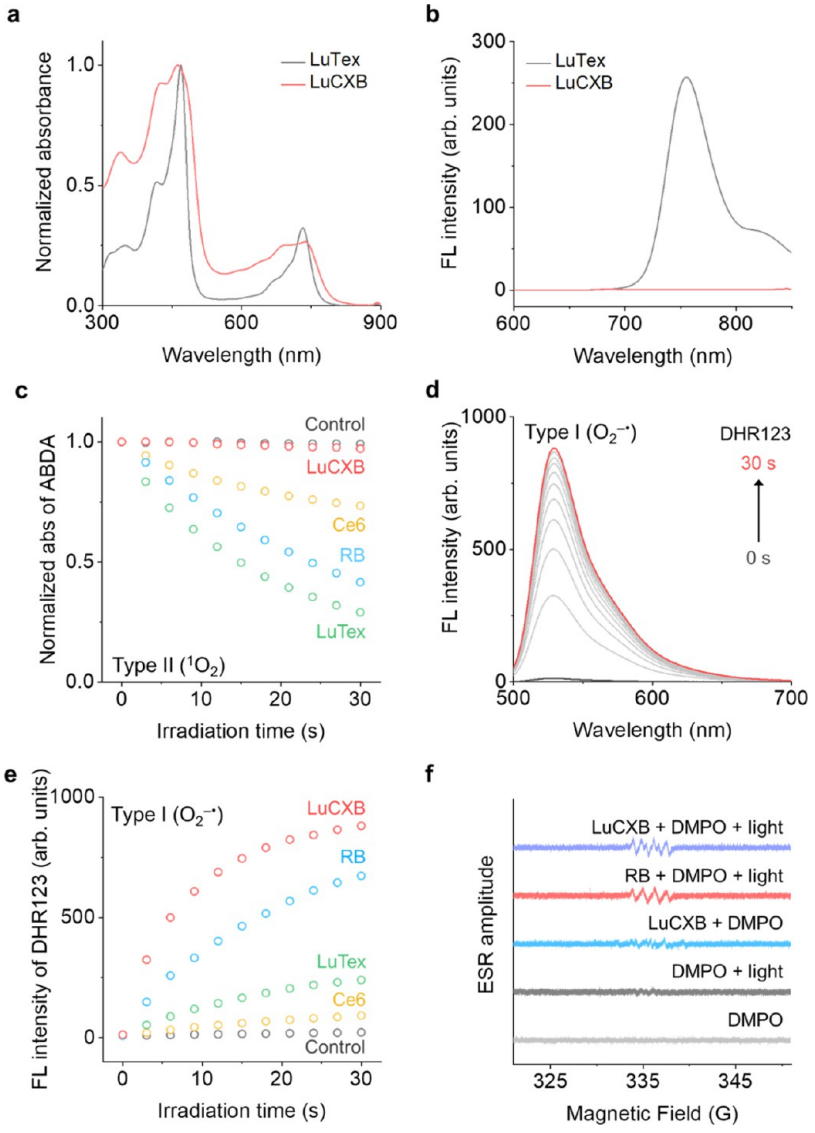

Figure 2. Studies of LuCXB as a potential type I photosensitizer. (a) UV−vis absorption and (b) fluorescence spectra of LuTex and LuCXB as recorded in phosphate-buffered saline (PBS, 10 mM, pH = 7.4) containing 1% dimethyl sulfoxide (DMSO) (v/v). Excitation wavelength: 480 nm. Slit widths: 5:5 nm. (c) Changes in the absorbance of 9,10-anthracenediyl-bis(methylene)dimalonic acid (ABDA, 100 μM) at 380 nm used as a probe for the singlet oxygen ($^1O_2$) when mixed with each of the indicated compounds in PBS containing 1% DMSO (v/v) (photosensitizer concentration = 5 μM) and subjected to photoirradiation for up to 30 s. Irradiation (100 mW/cm^2) was effected at 530 nm for Rose Bengal (RB), 660 nm for chlorin e6 (Ce6), and 730 nm for LuCXB and LuTex, respectively. (d) Superoxide radical ($O_2^{-\bullet}$) production by LuCXB (5 μM) as detected using dihydrorhodamine 123 (DHR123) (10 μM) as an indicator in PBS containing 1% DMSO (v/v). (e) Fluorescence response of DHR123 (10 μM) produced by the indicated photosensitizers (5 μM) in PBS containing 1% DMSO (v/v). (f) Electron spin resonance (ESR) spectral studies taken as evidence of $O_2^{-\bullet}$ generation by LuCXB (5 μM) under conditions of photoirradiation for 3 min (730 nm, 100 mW/cm^2). 5,5-Dimethyl-1-pyrroline *N*-oxide (DMPO) was used as an $O_2^{-\bullet}$ trap and RB (5 μM) was used as a positive control.

Information. Briefly, commercially available celecoxib (**1**) was converted in two steps to the key precursor **3**. LuTex (**4**) was synthesized following established literature procedures.[41,42] The LuTex-NH_2 derivative (**5**) was obtained from **4** via an optimized Mitsunobu procedure. The targeted compound LuCXB was then synthesized by reacting compound **3** with **5**. All new compounds were characterized by standard spectroscopic techniques and gave analytical data consistent with their proposed structures (Figures S1−S10).

The photophysical properties of LuCXB and LuTex (used as a reference) were assessed using ultraviolet−visible (UV−vis) and fluorescence spectroscopies. The absorption spectra of LuCXB and LuTex are both characterized by a broad Soret-like absorption maximum centered at approximately 480 nm and a weaker Q-type band at 730 nm in phosphate-buffered saline (PBS, 10 mM, pH = 7.4) containing 1% dimethyl sulfoxide (DMSO) (Figure 2a). While LuTex gives rise to a strong NIR fluorescence emission at 750 nm upon photoexcitation in this aqueous medium, this was not the case for LuCXB (Figure 2b). The lack of appreciable fluorescence seen for LuCXB is ascribed to photoinduced electron transfer (PeT) from the celecoxib moiety to the texaphyrin core, which serves to quench the excited state, as suggested in prior reports.[43−45]

Next, the ability of LuCXB to generate ROS in PBS (10 mM, pH = 7.4) was evaluated using 9,10-anthracenediyl-bis(methylene)dimalonic acid (ABDA) as a $^1O_2$-specific indicator and dihydrorhodamine 123 (DHR123) as a universal

https://doi.org/10.1021/jacs.4c05978
J. Am. Chem. Soc. XXXX, XXX, XXX−XXX

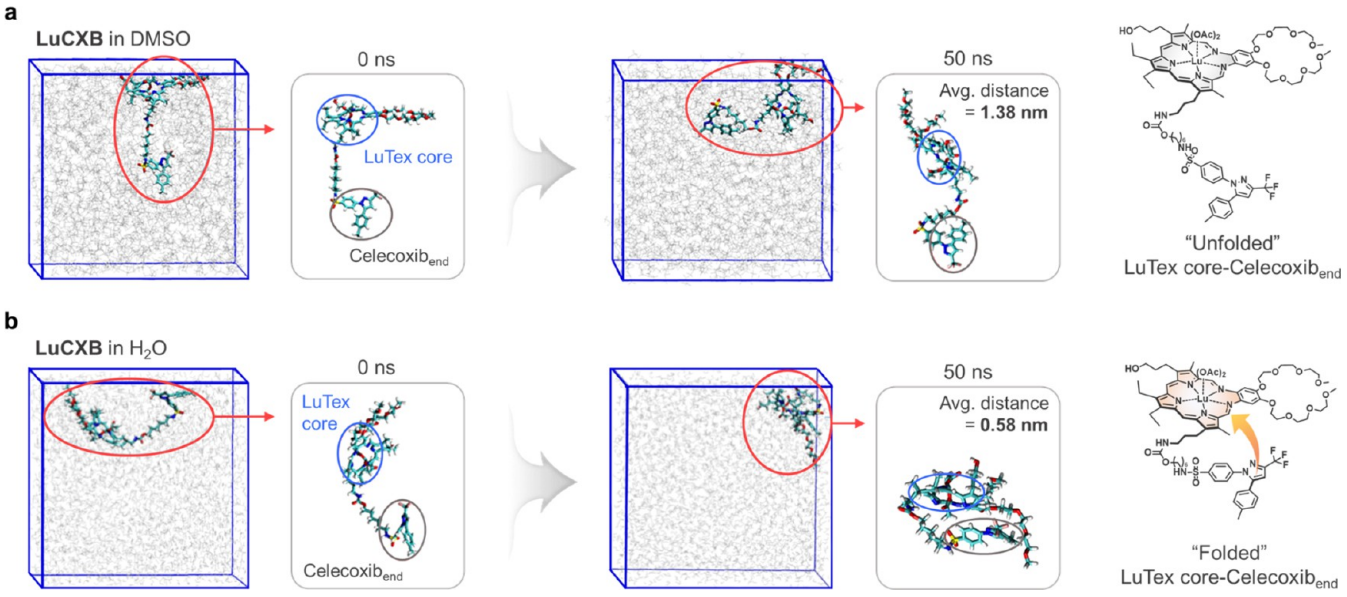

Figure 3. Initial conformation (left panel) of systems consisting of (a) LuCXB in DMSO and (b) LuCXB in H_2O. The corresponding conformations of the simulated systems (right panel), as obtained at the end of a 50 ns simulation performed at 300 K, are shown. (LuCXB is shown in the tube model, while the H_2O and DMSO solvents are shown in silver).

$O_2^{-\bullet}$ scavenger (Figure S11). Upon photoirradiation, the absorption of ABDA (100 μM) at 380 nm was seen to decrease rapidly (i.e., over the course of 0 to 30 s) in the presence of various photosensitizers, including LuCXB, LuTex, chlorin e6 (Ce6), and Rose Bengal (RB), in PBS containing 1% DMSO (λ_{ex} = 730 (LuCXB and LuTex), 660 (Ce6), and 530 (RB) nm, respectively) (Figures 2c, S12, and S13). Notably, LuCXB gave rise to negligible changes in the ABDA absorption, a finding interpreted in terms of poor $^1O_2$ generation (type II photosensitization) under conditions of photoirradiation in aqueous media. The $^1O_2$ generation quantum yield (Φ) of LuCXB was calculated using LuTex as the reference in accord with a standard method[46] and found to be less than 0.01. On the other hand, effective $O_2^{-\bullet}$ production, presumably via a type I photodynamic process, was observed for LuCXB, as evidenced by an enhancement in the fluorescence intensity of DHR123 under conditions of 730 nm photoillumination (Figure S14). A time dependence plot revealed that, in the case of LuCXB, $O_2^{-\bullet}$ generation is essentially complete within 30 s (Figures 2d and S15). LuTex exhibited notably reduced efficacy relative to LuCXB under identical photoirradiation conditions, whereas the efficacy of RB proved comparable (Figures 2e and S16). The production of each ROS was further confirmed through electron spin resonance (ESR) spectroscopic analysis using 5,5-dimethyl-1-pyrroline *N*-oxide (DMPO) as a trap for free radicals and 2,2,6,6-tetramethylpiperidine (TEMP) as a $^1O_2$ trap. This resulted in the formation of paramagnetic DMPO−OH$^\bullet$ and TEMP−$^1O_2$ adducts (Figures S17 and S18). In these studies, RB was used as a positive control. These findings are taken as evidence for the production of $O_2^{-\bullet}$ by LuCXB under conditions of photoirradiation (Figure 2f). Gratifyingly, LuCXB exhibited good stability, even when subject to intensive photoirradiation (Figures S19). The absorbance and fluorescence emission spectra of LuCXB were measured across the 1−12 pH range. The results revealed minimal changes within the 4−8 pH range; however, notable changes were observed when the pH was below 3 or above 9 (Figure S20). In the physiological pH range, LuCXB demonstrated minimal $^1O_2$ production (Figure S21), but notable $O_2^{-\bullet}$ generation, including at pH = 5, a pH value that mirrors the tumor microenvironment (Figure S22).

The photophysical properties of LuCXB were further investigated in different organic solvents of varying polarity (Figure S23). The maximum absorption wavelengths of LuCXB were measured as a function of solvent polarity as reported in the Catalán data set.[47] The maximum absorption wavelength of LuCXB gradually decreases as the solvent polarity increases (Figure S24). This observation is thought to reflect intramolecular aggregation-caused quenching arising from LuTex−celecoxib donor−acceptor interactions. The ROS generation efficiency of LuCXB was also measured in DMSO, an organic solvent that fully solvates the molecule, thus minimizing the intramolecular interactions between the LuTex core and the conjugated celecoxib moiety. Notably, the absorption profile pattern of LuCXB closely resembled that of LuTex, suggesting that the LuTex core in LuCXB does not interact with the conjugated celecoxib moiety in this solubilizing medium. This was expected to favor a type II, rather than type I, mechanism. In fact, a change in the absorption profile of 1,3-diphenylisobenzofuran (DPBF) at 417 nm was seen in the presence of LuCXB when subject to photoirradiation (730 nm, 0.1 mW/cm^2) (Figure S25). This is taken as evidence of $^1O_2$ generation as expected for a type II mechanism.

Given the inferred intramolecular interaction in aqueous media, we used surfactants to promote an environment capable of breaking up the intramolecular interactions in LuCXB, similar to what was achieved using DMSO as a solvent. Upon the addition of different surfactants, including Triton-X100 and Tween 20 in PBS, concentration-dependent changes in the absorption and fluorescence emission of LuCXB were observed (Figures S26−S28). On this basis, we conclude that the surfactants act to improve the aqueous solubility of LuCXB, thus decreasing the intramolecular interactions between the celecoxib moiety and the LuTex core.

https://doi.org/10.1021/jacs.4c05978
J. Am. Chem. Soc. XXXX, XXX, XXX−XXX

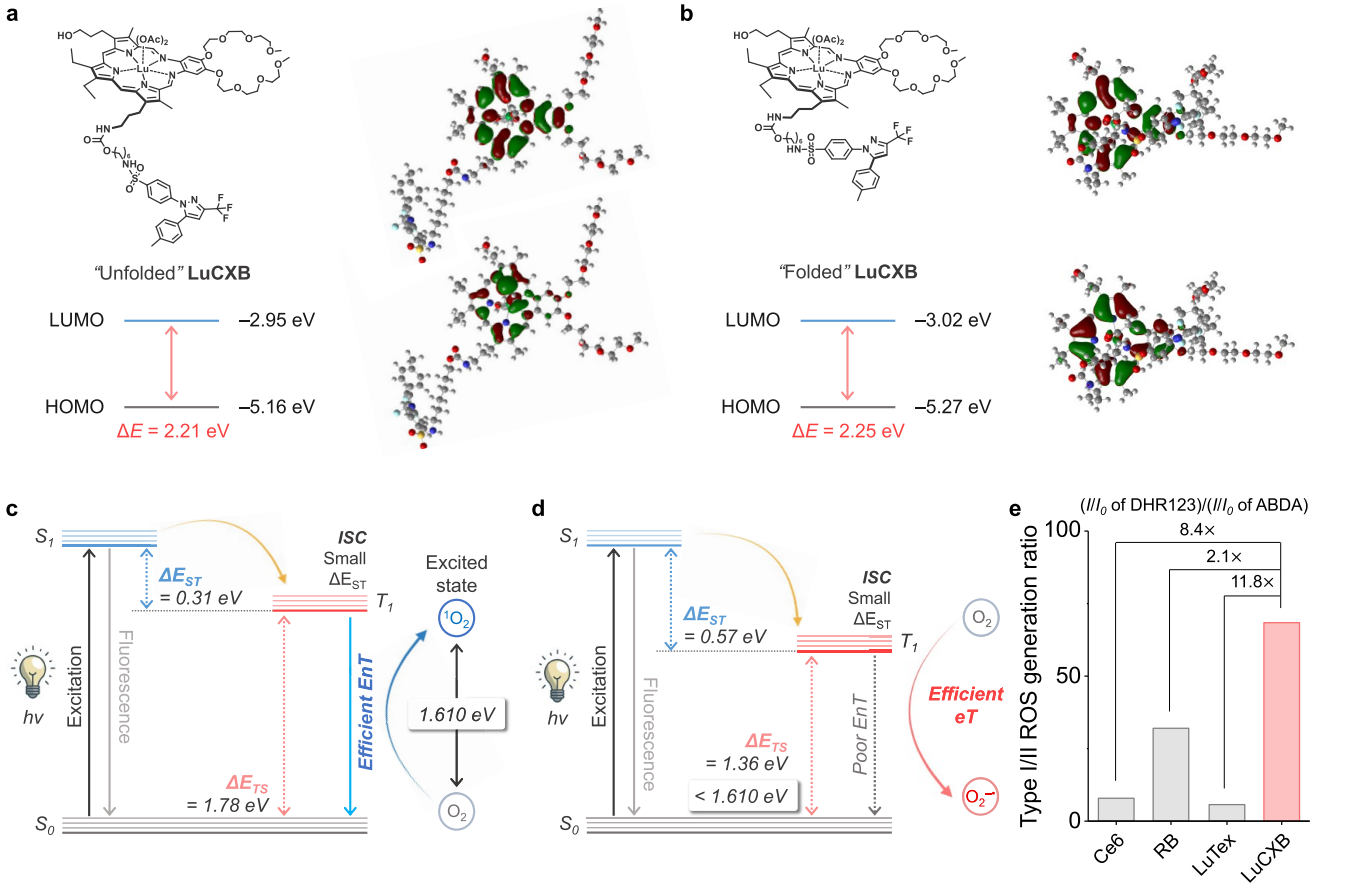

Figure 4. Density functional theory (DFT) calculations showing the optimized structures of unfolded and folded LuCXB systems. Frontier molecular orbitals and energies (eV) derived from DFT calculations of (a) unfolded and (b) folded LuCXB in their ground state. Calculated lowest excited singlet (S_1) and triplet energy (T_1) of (c) unfolded LuCXB and (d) folded LuCXB. (e) Relative ratio of type I and II ROS generation (efficiency) for Ce6, RB, LuTex, and LuCXB in PBS (10 mM, pH = 7.4) under conditions of 730 nm photoirradiation.

Next, the ability of LuCXB to photocatalyze $^1O_2$ production was studied using ABDA as the indicator in an aqueous PBS medium containing 1% DMSO and 1% Triton-X100. As expected for a system free of intramolecular interactions, LuCXB produced $^1O_2$ effectively when subject to 730 nm lamp irradiation (100 mW/cm^2) (cf. Figure S29). Under these conditions, the Φ of LuCXB was calculated to be 0.61 of that recorded in the case of LuTex (Figure S30).[46] Collectively, our findings lead us to suggest that under less polar conditions, intramolecular $\pi-\pi$ donor–acceptor interactions between the LuTex core and the celecoxib moiety are reduced, thus favoring a type II photodynamic pathway that produces $^1O_2$. Conversely, in more aqueous environments, LuCXB tends to generate $O_2^{-\bullet}$.

The effect of solvents on the putative intramolecular interactions of LuCXB was studied using two independent molecular dynamics simulations carried out in the presence of H_2O (polar protic) and DMSO (polar aprotic), respectively. Using the Packmol program, LuCXB was randomly arranged in a 5.0 × 5.0 × 5.0 nm^3 simulation box. The images of the initial and simulated conformations of LuCXB in H_2O and DMSO are shown in Figure 3 (left-initial and right-simulated). The conformations of LuCXB in the simulated form were markedly different from the corresponding initial states in both solvents. In H_2O, the simulated conformation of LuCXB was characterized by a folded structure, with the celecoxib$_{end}$ moiety close to the LuTex core. This folding is not seen in DMSO, where the LuCXB exists in an unfolded conformation.

The properties of LuCXB in two different solvent media were quantified via root-mean-square deviation (RMSD), root-mean-square fluctuation (RMSF), and average distance criteria.[48,49] To gain insights into the flexible nature of the molecule in both solvents, the RMSD of LuCXB was calculated from the trajectories generated after equilibration. The calculated average RMSD (⟨RMSD⟩) values of LuCXB in H_2O and DMSO were found to be 2.38 and 2.44 nm, respectively (Figure S31a). The lower RMSD value of LuCXB in H_2O is taken as a reflection of the reduced conformational flexibility, as expected for a system where stacking between the LuTex core and the celecoxib$_{end}$ moiety is favored. Similar conclusions were supported by the RMSF values. For instance, the RMSF values of LuCXB in H_2O and DMSO were 0.25 and 0.35, respectively (Figure S31b). Furthermore, the average distance between the LuTex core and the celecoxib$_{end}$ subunit in H_2O (0.58 nm) was less than that in DMSO (1.38 nm) (Figure S32). Again, this is consistent with LuCXB existing in a folded form in polar protic media.

Density Functional Theory Calculations. Molecular dynamics simulation results provided support for the suggestion that the LuCXB system would fold or unfold depending on the polarity of the solvent. Unknown from this analysis, however, was why the ROS, the putative folded and unfolded forms of LuCXB produced different classes of ROS.

https://doi.org/10.1021/jacs.4c05978
J. Am. Chem. Soc. XXXX, XXX, XXX−XXX

Table 1. Photophysical and Photosensitizing Properties of LuTex, Unfolded LuCXB, and Folded LuCXB

compound	λ_{abs} (nm)[c]	λ_{em} (nm)[c]	$\Delta\nu$ (nm)[f]	Φ_F[g]	Φ_{ROS}[h]	type I/II ratio[j]	HOMO (eV)[l]	LUMO (eV)[l]	E_g (eV)[m]	ΔE_{S1-T1} (eV)[n,o]	ΔE_{T1-S0} (eV)[n,p]
LuTex[a]	469[d]:733[e]	755	286[d]:22[e]	0.12	0.58[i]	5.8	−4.62	−2.99	1.63	0.73	n.c.
LuCXB (unfolded)[b]	470:733	756	286:23	0.13	0.61	n.c.[k]	−5.16	−2.95	2.21	0.31	1.78
LuCXB (folded)[a]	462:737	786	324:49	<0.01	<0.01	68.3	−5.27	−3.02	2.25	0.57	1.36

[a]In PBS (10 mM, pH = 7.4) containing 1% DMSO (v/v). [b]In PBS/Triton-X100 1% (v/v) containing 1% DMSO (v/v). [c]Concentration: 10 μM. [d]Soret band. [e]Q-band. [f]Stokes' shift. [g]Fluorescence quantum yield determined using tetraphenylporphyrin as the standard (Φ_F = 0.11 in methanol).[51] [h]$^1O_2$ generation quantum yield using LuTex as the standard. [i]Reported value.[29] [j]Ratio of the change in fluorescence intensity of DHR123 and the change in the absorption of ABDA seen as a function of time under conditions of photoirradiation. [k]n.c.: not calculated. [l]DFT calculations were performed with the B3LYP hybrid functional based on the SDD/6-31G(d) basis set, using the Gaussian 16 software package. [m]Energy difference between the HOMO and LUMO levels. [n]Time-dependent DFT (TD-DFT) calculations were carried out to determine the energy levels of the excited states using the same functional and basis set. [o]Energy difference between S_1 and T_1. [p]Energy difference between S_0 and T_1.

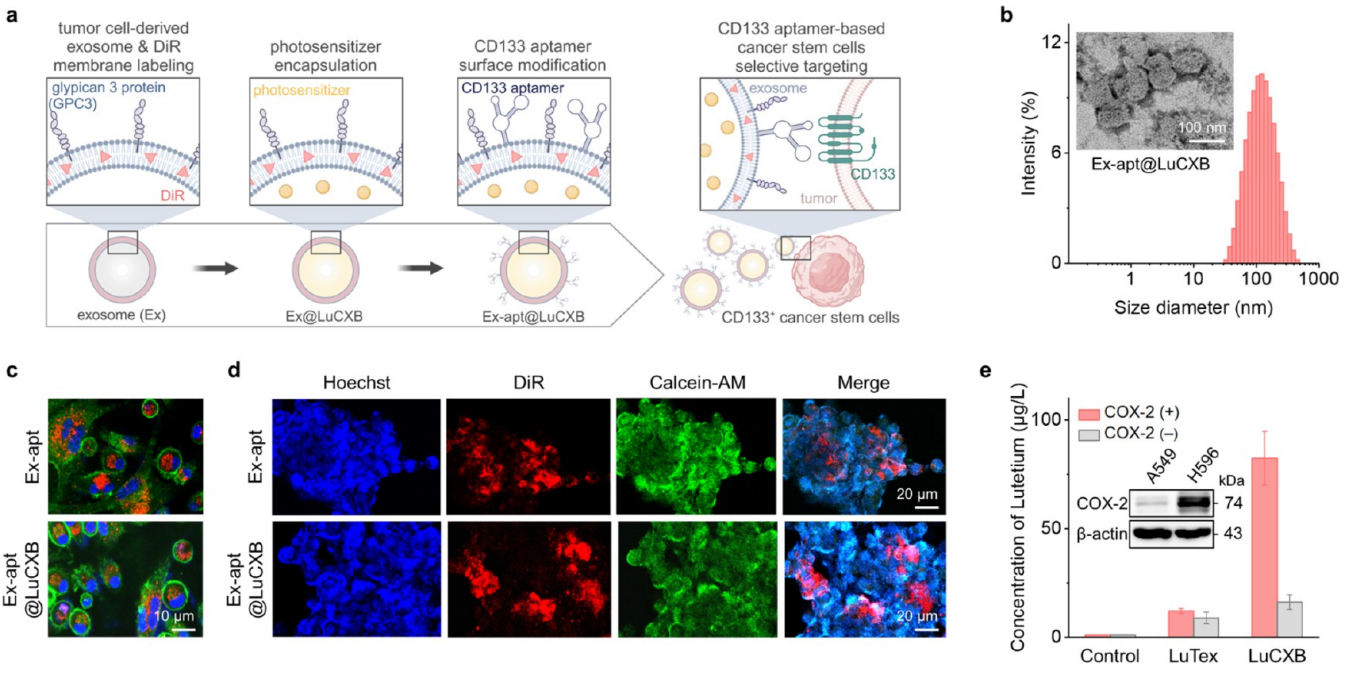

Figure 5. Preparation and characterization of LuCXB-based exosome nanophotosensitizer. (a) Summary of the procedure used to prepare the CD133 aptamer-decorated nanophotosensitizer, Ex-apt@LuCXB, and its tumor-targeting ability. (b) Dynamic light scattering (DLS) particle size distribution analysis of Ex-apt@LuCXB. The inset provides a transmission electron microscopy (TEM) image of the Ex-apt@LuCXB micrograph. Scale bars indicate the length stated in the figure (Scale bar: 100 nm). Cellular uptake of Ex-apt and Ex-apt@LuCXB in (c) bone marrow-derived dendritic cells and (d) Hepa1−6 liver cancer cells. Hoechst 33342-stained cell nuclei (blue color), Calcein-AM labeled cytosol of living cells (green color), and 1,1-dioctadecyl-3,3,3,3-tetramethylindotricarbocyanine iodide (DiR)-stained exosome membrane lipids (red color), respectively. Scale bars indicate the length stated in the figures. Scale bars: 10 μm (c) and 20 μm (d). (e) Concentration of lutetium(III) metal ions found after incubating with either LuTex or LuCXB for 24 h (10 μM, 37 °C) with H596 cyclooxygenase-2 (COX-2) positive (+ve) and A549 COX-2 negative (−ve) cells, as determined using a inductively coupled plasma mass spectrometer (ICP-MS). Inset: Western blotting determination of COX-2 expression levels in A549 and H596 cell lines. Data are represented by the mean ± the standard deviation (s.d.) derived from n = 3 independent experiments. Panel (a) was created with BioRender.com.

Therefore, time-dependent density functional theory (TD-DFT) calculations were performed. The conformations of LuTex, folded LuCXB and unfolded LuCXB systems were initially optimized. Their ground state (S_0), first singlet excited state (S_1), and first triplet excited state (T_1) energy levels were then calculated (Figures 4a,b, and S33−S35). For type I electron transfer, the interaction between the triplet state population of the photosensitizer (produced via an intersystem crossing (ISC) process) and the triplet ground state of oxygen molecules plays a critical role. The equation below was used to estimate the ISC rate of the compounds.[8,50]

$$k_{ISC} = \propto \frac{\langle T_1|H_{SO}|S_1\rangle^2}{(\Delta E_{S_1-T_1})^2}$$

where H_{SO} is the Hamiltonian for the spin−orbit coupling, and ΔE_{S1-T1} represents the energy difference between the S_1 and T_1 states. According to this equation, the ISC rate is inversely proportional to the square of ΔE_{S1-T1}. The calculated energy differences for various conformers of LuCXB and LuTex are provided in Table 1. The ΔE_{S1-T1} values of the unfolded and folded LuCXB states (0.31 and 0.57 eV, respectively) were found to be smaller than that of LuTex (0.73 eV) (Figure

https://doi.org/10.1021/jacs.4c05978
J. Am. Chem. Soc. XXXX, XXX, XXX−XXX

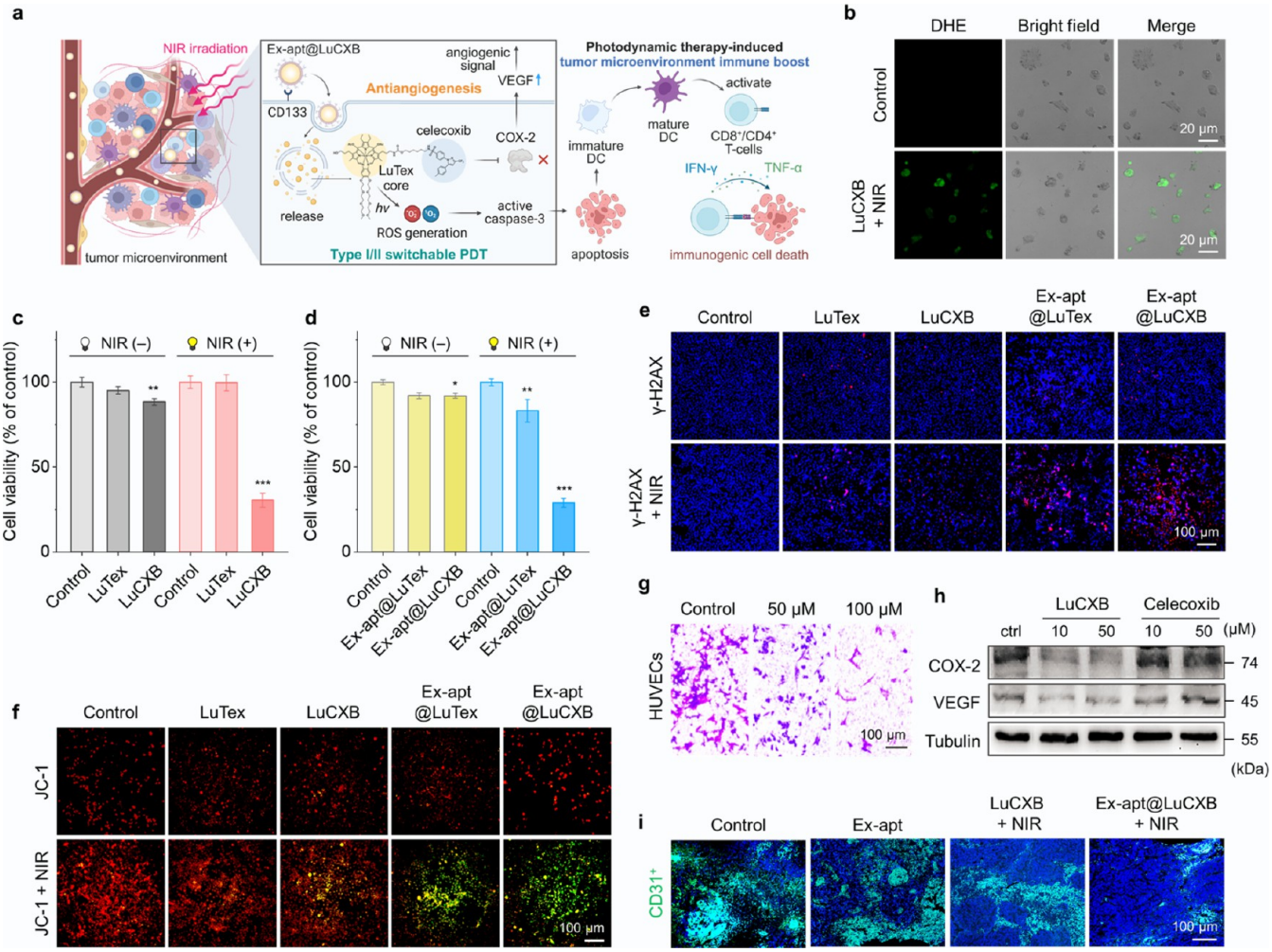

Figure 6. In vitro evaluation of the biocompatibility and photodynamic anticancer effect of Ex-apt@LuCXB. (a) Illustration of a proposed synergistic anticancer effect comprising (1) type I/II switchable ROS-induced damage; (2) antiangiogenesis; and (3) tumor microenvironment immune boost. (b) Confocal laser scanning microscopy (CLSM) images corresponding to intracellular $O_2^{-\bullet}$ production in Hepa1−6 cells that were preincubated with LuCXB followed by incubation with dihydroethidium (DHE) as an $O_2^{-\bullet}$ indicator (10 μM) as recorded in the absence or presence of 730 nm lamp photoirradiation (100 mW/cm^2, 1 min). Scale bar: 20 μm. Relative viability of Hepa1−6 cells as determined by CCK-8 assays for (c) LuTex and LuCXB, and (d) exosome-based nanophotosensitizers (Ex-apt@LuTex and Ex-apt@LuCXB) relative to control (1% DMSO). After photoirradiation for 10 min (730 nm, 100 mW/cm^2), the CCK-8 assay was used to determine the photodynamic effect in the Ex-apt@LuTex and Ex-apt@LuCXB treatment groups in Hepa1−6 cells. Data are represented by mean ± s.d. (n = 5 independent experiments). ***p < 0.001, **p < 0.01, *p < 0.05. Fluorescence images of (e) γ-H2AX (DNA fragmentation) and (f) JC-1 (mitochondrial apoptosis) in Hepa1−6 cells for the indicated treatment groups. All groups involving near-infrared (NIR) photoirradiation were irradiated with a 730 nm laser (100 mW/cm^2, 10 min). Scale bar: 100 μm. (g) Hematoxylin and eosin (H&E) staining of human umbilical vein endothelial cells (HUVECs) after treatment with LuCXB (0, 50, and 100 μM). Scale bar: 100 μm. (h) Protein expression levels of COX-2 and vascular endothelial growth factor (VEGF) in Hepa1−6 cells. Western blot showing endogenous COX-2 and VEGF expression levels after treatment separately with LuCXB or celecoxib (0, 10, and 50 μM). (i) Immunohistochemical fluorescence of CD31-positive cells (green color) in tumor tissues as observed by CLSM. DAPI was used to stain the cellular nuclei (blue color). Scale bar: 100 μm. Panel (a) was created with BioRender.com.

4c,d). More efficient ISC and enhanced ROS generation were thus expected for LuCXB than for LuTex.

Next, the energy levels of the S_0/T_1 states of the photosensitizer, triplet oxygen ($^3O_2$), and $^1O_2$ were calculated in an effort to determine whether an electron transfer (type I) or energy transfer (type II) pathway would be preferred. It is well-known that if the ΔE_{T1-S0} values of a photosensitizer are smaller than the $^3O_2-^1O_2$ spin state conversion energy gap (1.61 eV), the energy transfer process is thermodynamically disfavored.[8,50] As shown in Table 1, the unfolded LuCXB system exhibited a ΔE_{T1-S0} value (1.78 eV) that is greater than 1.61 eV; conversely, the folded LuCXB conformation was characterized by a smaller value (1.36 eV) (Figure 4c,d). The results of the simulations proved concordant with the experimental data. For instance, the use of LuCXB led to exclusive $^1O_2$ generation in DMSO but effective $O_2^{-\bullet}$ production in an aqueous medium. The 11.8-fold type I/II ROS generation ratio of LuCXB in aqueous media with respect to LuTex is taken as evidence that LuCXB can be used to produce $O_2^{-\bullet}$ effectively, in contrast to what is seen for LuTex (Figure 4e). Given the potential anticancer benefits of $O_2^{-\bullet}$ production, an effort was thus made to test the utility of LuCXB as a photosensitizer in vitro and in vivo.

Preparation and Characterization of Nanophotosensitizer Ex@LuCXB. For IPDT studies, cancer cell-derived exosomes were prepared and used as carriers for LuCXB

https://doi.org/10.1021/jacs.4c05978
J. Am. Chem. Soc. XXXX, XXX, XXX−XXX

(Figure 5a).[52] Exosomes derived from the supernatant of Hepa1−6 tumor cells, a mouse liver cancer cell line, were extracted via ultracentrifugation (100,000*g*). In accordance with previous reports, tumor-derived exosomes present a range of tumor-specific antigens. Western blot studies confirmed that the specific Hepa1−6-derived exosomes used in the present study bear a large quantity of liver cancer-specific antigens, namely glypican 3 proteins (GPC3), on the surface of the lipid membrane (Figure S36a). To determine the localization of exosomes after treatment, the as-prepared exosomes were incubated with 1,1-dioctadecyl-3,3,3,3-tetramethylindotricarbocyanine iodide (DiR), a NIR cyanine dye; this was done due to the poor fluorescence quantum yield of LuCXB under physiological conditions (Φ_F < 0.01). Next, LuCXB was incorporated into the cancer cell-derived exosomes via ultrasonication of a LuCXB-exosome mixture following an established protocol.[36] The resulting constructs, referred to as Ex@LuCXB, were further functionalized with a CD133-targeting aptamer, resulting in the formation of Ex-apt@LuCXB (Figure 5b).[40,53,54] Exosomes functionalized with the CD133 aptamer but free of the LuCXB photosensitizer (Ex-apt) were prepared as a control. The diameter of the Ex-apt was found to be 100 nm as determined via dynamic light scattering (DLS) and transmission electron microscopy (TEM) analyses (Figure S36b). The corresponding diameter of the exosomes containing LuCXB was approximately 10 nm larger (Figure 5b).

To determine the cellular uptake of Ex-apt and Ex-apt@LuCXB, fluorescence images of live murine bone marrow-derived dendritic cells (DC) were obtained after the cells were cocultured with Ex-apt or Ex-apt@LuCXB for 24 h. The resulting images revealed internalization of Ex-apt and Ex-apt@LuCXB, as inferred from the DiR-derived fluorescent signature. To allow valid comparisons, Calcein-AM was used to label the cytoplasm of the cells (Figures 5c and S37). Furthermore, as can be seen from Figure 5d, cellular uptake of both Ex-apt and Ex-apt@LuCXB is readily apparent in the case of Hepa1−6 cells. We thus conclude that tumor cells are able to take up Ex-apt@LuCXB and that the latter constructs should act as an effective nanophotosensitizer.

Celecoxib-Driven Cellular Guiding and Accumulation Behavior of LuCXB. Further support for the proposed localizing features came from studies involving two different lung cancer cell lines, namely H596 and A549. These two cell lines were chosen because elevated COX-2 expression levels have been observed in H596 cells, whereas A549 cells exhibit negligible COX-2 expression levels. They were thus expected to function as COX-2 positive (+ve) and negative (−ve) models, respectively (inset to Figure 5e). As shown in Figure 5e, inductively coupled plasma mass spectrometry (ICP-MS) analyses were used to quantify the lutetium(III) cation levels in the corresponding cellular lysates. LuCXB exhibited a significantly high concentration in COX-2 (+ve) cells (82.4 μg/L) as compared to the negative (−ve) model (16.2 μg/L). In contrast, treatment with free LuTex led to little accumulation of lutetium(III) in either the COX-2 (+ve, 12.2 μg/L) or COX-2 (−ve, 8.9 μg/L) cells. This supports the design expectation that LuCXB, composed of a celecoxib moiety linked to a LuTex core, is located well into cancer cells where COX-2 is upregulated. Docking simulations were then carried out in an effort to obtain insights into the binding interactions between COX-2 and LuCXB at the atomic level. Based on these studies (Figure S38), LuCXB is located in the cleft region of COX-2 and bound favorably (binding free energy = −71.3 kcal/mol).

Biosafety and ROS-Generation Efficiency of LuCXB. Next, the anticancer effects of LuCXB-based on ROS-induced photodamage, antiangiogenesis, and immunogenic tumor cell suppression were examined. The experimental design is summarized in Figure 6a. Initially, the production of ROS induced by LuCXB was measured under light irradiation in Hepa1−6 liver cancer cells. For this portion of the study, Hepa1−6 cells were preincubated first with LuCXB, followed by dihydroethidium (DHE), a known $O_2^{-\bullet}$ indicator. The Hepa1−6 cells preincubated with LuCXB gave rise to intense green confocal laser scanning microscopy (CLSM) images in the DHE channels under 730 nm lamp irradiation (100 mW/cm^2, 1 min); this was considered indicative of ROS generation, especially type I $O_2^{-\bullet}$ generation (Figure 6b).

The photocytotoxicity of LuCXB was assessed in Hepa1−6 cells as a function of photosensitizer concentration. For this study, Hepa1−6 cells were preincubated with LuTex and LuCXB, respectively, and the cell viability assay was evaluated without or with NIR photoirradiation (730 nm, 100 mW/cm^2, 10 min). Both texaphyrins displayed negligible cytotoxicity in the absence of photoirradiation (Figure S39a). Upon photoirradiation, LuCXB produced a high level of cytotoxicity, while less pronounced phototoxic effects were observed using LuTex under identical photoirradiation conditions (Figures 6c and S39b). The phototoxicities of Ex-apt@LuTex and Ex-apt@LuCXB were slightly enhanced relative to the free forms with negligible dark toxicity again being observed (Figure S40a). Mirroring what was seen for LuTex and LuCXB, upon photoirradiation, Ex-apt@LuCXB gave rise to a greater level of phototoxicity than Ex-apt@LuTex (Figures 6d and S40b).

Next, Hepa1−6 cells incubated with LuTex, LuCXB, Ex-apt@LuTex, or Ex-apt@LuCXB, respectively, were stained to visualize DNA fragmentation via a γ-H2AX assay where live and apoptotic cells appear blue and red, respectively. γ-H2AX labeling revealed that NIR photoirradiation in conjunction with Ex-apt@LuCXB causes DNA damage at a higher level than seen with Ex-apt@LuTex (Figure 6e). When tested without exosome encapsulation, neither LuTex nor LuCXB produced significant DNA damage even under conditions of photoirradiation; presumably, this reflects less effective cellular uptake.

Phototoxicity-induced mitochondrial apoptosis was measured using the JC-1 assay. The phototherapeutic effect of Ex-apt@LuTex and Ex-apt@LuCXB caused the depolarization of mitochondrial membrane potentials as inferred from red and green labeling for live and dead cells, respectively (Figure 6f). Such findings are consistent with an apoptosis-induced cell death mechanism. We thus conclude that cellular ROS production from LuCXB, particularly via a type I $O_2^{-\bullet}$ photogeneration mechanism, induces photocytotoxic effects and leads to apoptosis in Hepa1−6 liver cancer cells under conditions of NIR irradiation.

Antiangiogenic Effect of COX-2 Inhibition. While therapeutic outcomes of PDT are often curative, incomplete PDT can trigger neovascularization and allow for tumor recurrence, effects potentially induced through tumor angiogenesis. Additionally, PDT-induced oxidative stress can result in hypoxic tumors. This, in turn, can lead to the expression of angiogenic growth factors and cytokines as an adaptive response through activation of signaling cascades, such as the hypoxia-signaling pathway and VEGF, which initiates angio-

https://doi.org/10.1021/jacs.4c05978
J. Am. Chem. Soc. XXXX, XXX, XXX−XXX

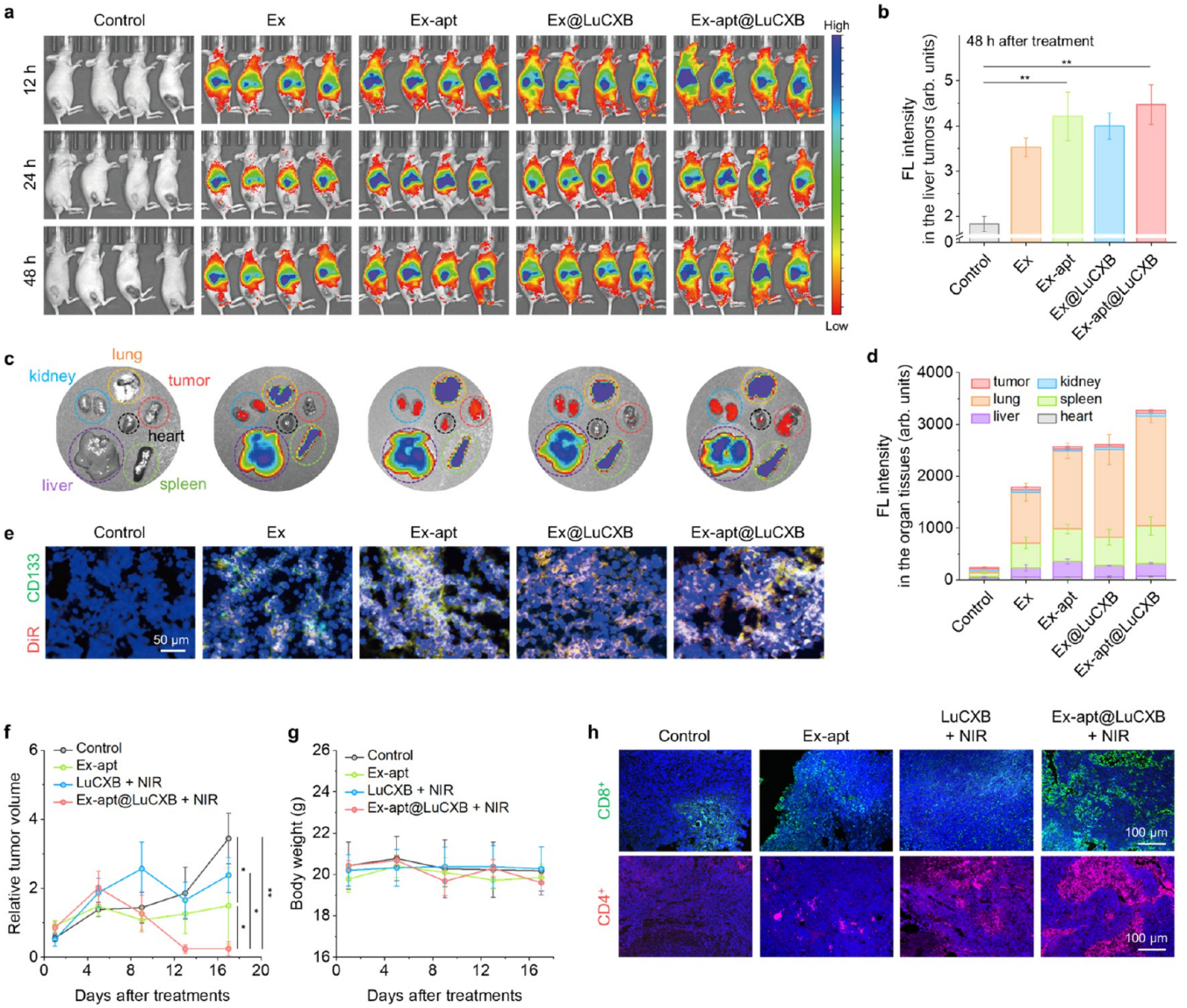

Figure 7. In vivo liver tumor (Hepa1−6) targeting and immune boost-based therapeutic effects of Ex-apt@LuCXB. (a) Live imaging of a subcutaneous Hepa1−6-bearing BALB/c nude mice model as assessed in different treatment groups (control, Ex, Ex-apt, Ex@LuCXB, and Ex-apt@LuCXB, respectively). Exosomes were labeled with the DiR dye, and the fluorescence intensity was recorded at 12, 24, and 48 h after tail vein injection. (b) Statistical analysis of tumor fluorescence intensity at 48 h postinjection. Error ranges are represented as s.d. (n = 4 biologically independent animals). $^{**}p < 0.01$. (c) Ex vivo fluorescence images of the liver tumor and main organs (kidneys, lungs, spleen, liver, and heart) recorded at 48 h postinjection. (d) Semiquantitative biodistribution of exosome-based nanodrugs, including Ex@LuCXB and Ex-apt@LuCXB, as determined from the average fluorescence intensity per gram of tumors and main organs. Error ranges represent s.d. derived from n = 4 independent experiments. (e) Immunofluorescence histochemical analysis of cancer stem cell-targeting Ex-apt@LuCXB in mouse liver cancer tissues. CD133-positive cancer stem cells are stained with CD133-FITC antibodies (green color), exosomes are stained with the DiR dye (red color), and the cellular nuclei are stained with DAPI (blue color). Scale bar: 50 μm. (f) Statistical analysis of the time-dependent tumor volume changes seen after treatment in each mouse group as monitored for 18 days. (g) Time-dependent body weight curves for animals subjected to different treatment regimens for 18 days. Data are represented as the mean ± s.d. (n = 4 biologically independent animals). $^{**}p < 0.01$, $^{*}p < 0.05$. (h) Immunohistochemical fluorescence of CD8 (green color) and CD4 (red color) positive cells in tumor tissues observed by CLSM. DAPI was used to stain the cellular nuclei (blue color). Scale bar: 100 μm.

genesis. Thus, we were keen to see whether LuCXB would act as a COX-2 inhibitor and inhibit VEGF pathways since this might improve antiangiogenic activity during PDT. To test this possibility, human umbilical vein endothelial cells (HUVECs) and Hepa1−6 cells were indirectly cocultured using a transwell system in a LuCXB-treated medium (Figure S41a). Treatment with LuCXB resulted in a decreased growth rate of HUVECs in a dose-dependent manner (Figure 6g). Additionally, Western blot analyses confirmed that treatment with LuCXB downregulated COX-2 expression levels in this Hepa1−6 cell-based test while simultaneously decreasing VEGF production relative to celecoxib (Figures 6h and S41b).

We also recorded the expression levels of CD31 angiogenesis factors in Hepa1−6 cells under Ex-apt@LuCXB-induced therapeutic conditions. Immunohistochemical fluorescence monitoring of the CD31 marker revealed that Ex-apt@LuCXB treatment induced suppression of microvessel density as manifested by a lowered green fluorescence response

https://doi.org/10.1021/jacs.4c05978
J. Am. Chem. Soc. XXXX, XXX, XXX−XXX

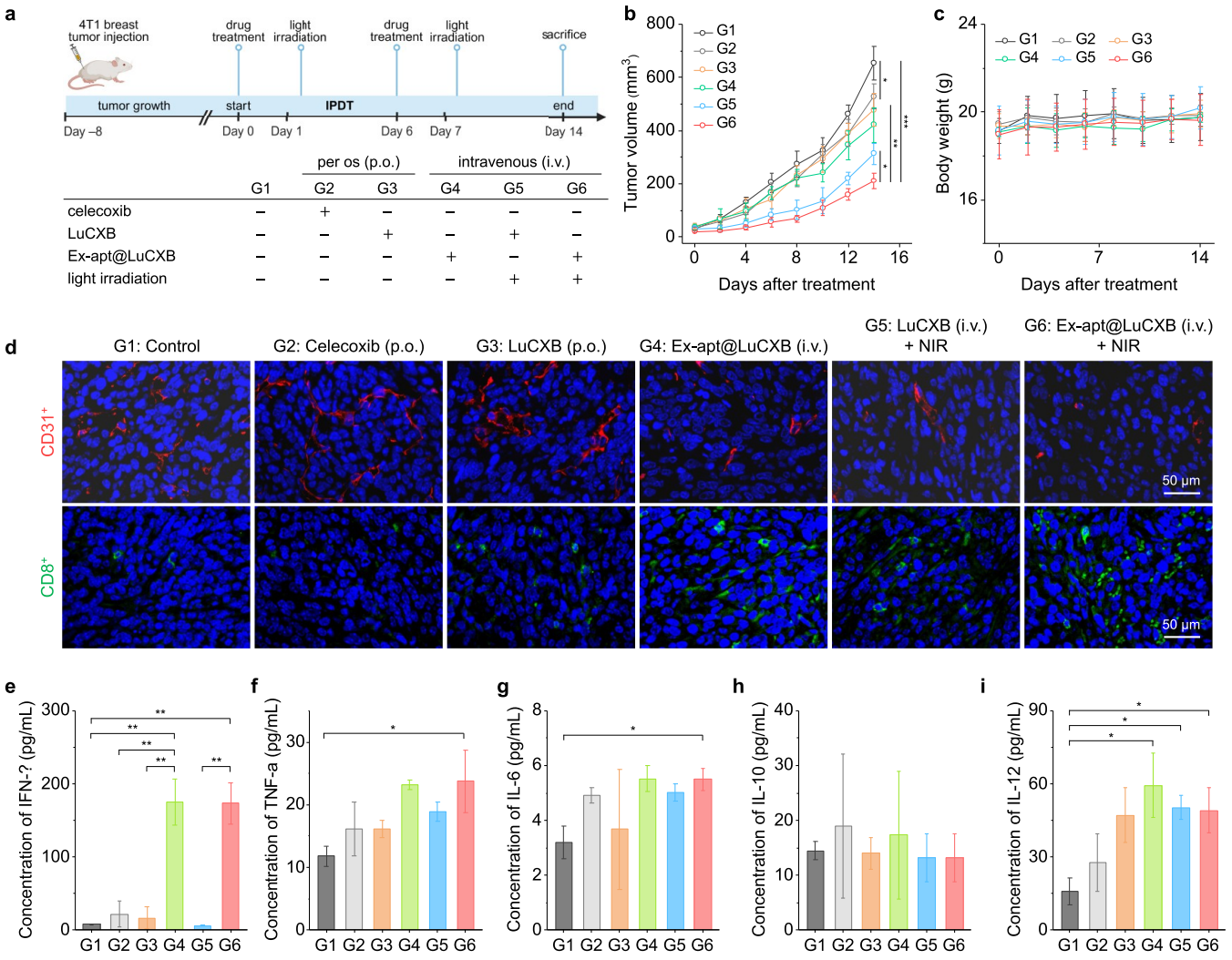

Figure 8. Photodynamic tumor suppression effect of Ex-apt@LuCXB and activation of an anticancer immunity response in a 4T1 mouse breast cancer model. (a) Schematic illustration of a therapeutic IPDT treatment procedure with different groups (control, celecoxib, LuCXB, and Ex-apt@LuCXB), respectively, administered per os (p.o.) or intravenous (i.v.) injection with or without NIR irradiation based on synergistic IPDT/antiangiogenesis in vivo. Flowchart for the establishment of a subcutaneous tumor model in BALB/c mice (4T1) and its use for each treatment group. (b) Time-dependent tumor volume changes and (c) body weight curves for different treatment groups for 14 days. Data points and error bars represent the mean value ± the s.d. based on n = 5 experiments involving biologically independent animals. ***$p < 0.001$, **$p < 0.01$, *$p < 0.05$. (d) Immunohistochemical fluorescence of regressive vasculature as determined using a CD31 marker (red color) and CD8$^+$ T cells (green color) in tumor tissues observed by CLSM. DAPI was used to stain the cellular nucleus (blue color). Scale bars: 50 μm. Quantitative analysis of serum Th-1 cytokines, including (e) interferon-γ (IFN-γ), (f) tumor necrosis factor-α (TNF-α), (g) interleukin (IL)-6, (h) IL-10, and (i) IL-12 in different mouse groups over 14 days based on an enzyme-linked immunosorbent assay (ELISA). Data represent the mean ± s.d. as derived from studies of $n = 5$ biologically independent animals. **$p < 0.01$, *$p < 0.05$. Panel (a) was created with BioRender.com.

(Figure 6i). LuCXB without the exosome nanocarrier produced a slightly lower antiangiogenic effect, presumably as a result of less efficient intracellular localization. In contrast, the control group and Ex-apt exhibited significant green fluorescence response, indicating high CD31 expression. Taken in concert, these findings support the conclusion that photoirradiation of Ex-apt@LuCXB leads to a decrease in COX-2 expression levels and lowered VEGF production, as well as suppression of angiogenesis.

Liver Cancer Stem Cell-Targeting and Immune Boost Effect of Ex-apt@LuCXB. Based on the above in vitro findings, an effort was made to evaluate the in vivo tumor localization and therapeutic effects of the photosensitizers in this study. With this goal in mind, BALB/c nude mice bearing Hepa1−6-induced liver cancers were injected intravenously with Ex, Ex-apt, Ex@LuCXB, or Ex-apt@LuCXB, and the biodistribution was examined by fluorescence live imaging. It was found that the red fluorescence response from DiR in the tumor-bearing mice gradually increased over time, with monitoring at 12, 24, and 48 h (Figure 7a). A statistical fluorescence intensity analysis confirmed the proposed enhanced targeting capability of the exosomes after aptamer surface modification presumably because of interactions with CD133, a common cancer stem cell marker in a wide variety of tumors (Figure 7b).

Ex vivo fluorescence images of the tumor and major organs (e.g., kidney, lung, spleen, liver, and heart) revealed that the aptamer-modified exosomes localized in the tumor region 48 h postinjection (Figure 7c). Statistically, Ex-apt@LuCXB was found to exhibit tumor-localization capability (Figure 7d). In

https://doi.org/10.1021/jacs.4c05978
J. Am. Chem. Soc. XXXX, XXX, XXX−XXX

addition, the targeting of Ex-apt@LuCXB to $CD133^+$ liver cancer stem cells was observed using frozen sections of tumors. As shown in Figure 7e, aptamer-modified DiR-labeled exosomes (red color) demonstrated apparent colocalization with cancer stem cells marked by the CD133-FITC antibody (green color). In contrast, DiR-labeled exosomes without the aptamer (Ex) produced negligible red-emissive fluorescence in the CD133 marker region. Collectively, these results are taken as evidence that exosome surface modification with CD133 aptamers (Ex-apt and Ex-apt@LuCXB) leads to effective targeting of $CD133^+$ cancer stem cells in Hepa1−6-induced liver cancer tissues.

Finally, the in vivo antitumor capability of Ex-apt@LuCXB was investigated in a mouse liver cancer model. The liver tumor model was established in B6 mice using Hepa1−6 cells. The mice were then divided into 4 groups and subjected to different treatments via intravenous (i.v.) injection: Control (PBS), Ex-apt, LuCXB + NIR, and Ex-apt@LuCXB + NIR groups, respectively. The time-dependent tumor volume changes in each mouse group were observed for 18 days (Figure 7f). Statistically significant tumor growth inhibition was seen in the mice treated with Ex-apt@LuCXB + NIR (730 nm, 100 mW/cm^2) without abnormal body weight changes (Figure 7g). At the end of the therapeutic course, almost all tumors were eliminated without relapse. Treatment with Ex-apt also produced noticeable tumor growth inhibition, leading us to suggest that the CD133 aptamer-decorated exosomes could induce an antitumor immunotherapeutic effect even in the absence of PDT. Immunohistochemical fluorescence analyses of CD8 and CD4 revealed that tumor tissues were in an immune-activated state. In contrast to the control and Ex-apt groups, tumor treatment with LuCXB and Ex-apt@LuCXB and NIR light (730 nm, 100 mW/cm^2) produced a higher infiltration of $CD8^+$ and $CD4^+$ T cells as inferred from an increase in green and red fluorescence, respectively (Figure 7h).

Antitumor Effect of Ex-apt@LuCXB in a 4T1 Mouse Breast Cancer Model. Prompted by the successful IPDT results in the liver cancer mouse model, the antitumor effect of Ex-apt@LuCXB was further explored in a breast cancer model. In these in vivo experiments, exosomes derived from 4T1 breast cancer cells were modified with CD133 aptamer to target $CD133^+$ breast cancer stem cells. The 4T1-tumor-bearing BALB/c mice were divided into 6 groups with different treatments and administration routes, namely per os (p.o.) or i.v. injection: (1) Control (PBS i.v. injection), (2) celecoxib (p.o.), (3) LuCXB (p.o.), (4) Ex-apt@LuCXB (i.v.), (5) LuCXB (i.v.) ± NIR irradiation, and (6) Ex-apt@LuCXB (i.v.) ± NIR irradiation, respectively (Figure 8a). After 14 days of treatment, individual tumor volumes in the different groups were measured, as shown in Figure 8b. Compared with the control group (G1), tumors in the mice treated orally with celecoxib (G2) or LuCXB (G3) were slightly inhibited, presumably due to the antiangiogenic tumor growth retardation. The group subjected to i.v. administration of Ex-apt@LuCXB without light irradiation (G4) demonstrated a moderate therapeutic benefit, a finding ascribed to an inherent immunogenic antitumor effect. In contrast, the CD133 aptamer-modified Ex-apt@LuCXB group exhibited excellent biocompatibility and tumor cytotoxicity under conditions of NIR photoirradiation (730 nm, 100 mW/cm^2) (G6), as compared to the corresponding LuCXB + NIR group (G5). None of the mice used in the study (i.e., across all groups) displayed abnormal body weight changes (Figure 8c). A histological analysis, including CD31 and $CD8^+$ T cell staining, provided evidence for an antiangiogenesis effect, as well as a higher level of tumor microenvironment infiltration; these latter findings are ascribed to an IPDT effect produced by LuCXB under conditions of photoirradiation (G4−G6) (Figure 8d).

In addition, serum cytokines in different mouse groups were detected via an enzyme-linked immunosorbent assay (ELISA). Mouse serum was collected from the breast cancer model animals after each treatment. The quantity of cytokines in the supernatant was determined, including interferon-γ (IFN-γ), tumor necrosis factor-α (TNF-α), interleukin (IL)-6, IL-10, and IL-12. The CD133 aptamer-decorated exosome-treated groups (G4 and G6) showed increased IFN-γ levels regardless of whether or not the animals were subjected to photoirradiation (Figure 8e). Relative to the control group (G1), each treatment increased the TNF-α levels, as shown in Figure 8f. Based on the immune response, presumably generated by the CD133 aptamer and LuCXB-induced IPDT, IL-6, and IL-12 were found to be upregulated in each treatment group; in contrast, negligible differences were observed for IL-10 (Figure 8g−i). Collectively, these results provide support for the premise underlying this study, namely that effective tumor localization provided by tumor-derived exosomes with CD133 aptamer surface modification, improved antiangiogenesis from LuCXB IPDT, and enhanced cancer stem cell targeting with immune activation leads to near-complete cancer cell eradication. A statistically significant reduction in tumor burden is also seen in vivo based on studies with mouse models.

CONCLUSIONS

This study was undertaken to explore whether structural refinement of LuTex to favor type I $O_2^{-\bullet}$ generation under photoillumination conditions would enhance IPDT efficacy. A desire to test this possibility led to the synthesis of the SMPC, LuCXB, wherein a LuTex core is conjugated with celecoxib. Both experimental and theoretical investigations confirmed that intramolecular donor−acceptor interactions between the LuTex core and the celecoxib moiety effectively reduce the singlet−triplet energy gap (ΔE_{T1-S0}), which bolsters the production of $O_2^{-\bullet}$. Cancer cell targeting of COX-2 by the celecoxib component facilitates tumor-specific localization, minimizing the risk of off-target photoactivation during treatment. Furthermore, LuCXB exhibits a chemotherapeutic effect, particularly in antiangiogenesis, enhancing the overall PDT efficacy. For therapeutic applications in vitro and in vivo, CD133-targeting, aptamer-decorated exosomes were employed as carriers to deliver LuCXB as a payload directly to liver and breast cancer cells. Integrating LuCXB with these exosome-based delivery systems (to give Ex-apt@LuCXB) led to improved targeting specificity, enhanced biocompatibility, and reduced systemic toxicity. The ability of these exosomes to target cancer stem cells boosts the therapeutic efficacy and reduces off-target effects, features that are deemed beneficial for IPDT. Consistent with these design expectations, we found that Ex-apt@LuCXB demonstrated good antitumor efficiency in both cell culture and mouse models, while also appearing to reduce tumor stemness. Based on the present findings, we believe that SMPCs such as LuCXB will have a role to play in IPDT-based cancer therapies, particularly in targeting and ablating cancer stem cells.

https://doi.org/10.1021/jacs.4c05978
J. Am. Chem. Soc. XXXX, XXX, XXX−XXX

MATERIALS, INSTRUMENTS, AND METHODS

For details, see the Supporting Information.

ASSOCIATED CONTENT

Supporting Information

The Supporting Information is available free of charge at https://pubs.acs.org/doi/10.1021/jacs.4c05978.

Detailed experimental conditions and methods, synthesis, structural characterization, functional characterization, biological evaluations, schemes S1−S4, and figures S1−S41 (PDF)

AUTHOR INFORMATION

Corresponding Authors

Jin Yong Lee − *Department of Chemistry, Sungkyunkwan University, Suwon 16419, Korea;* orcid.org/0000-0003-0360-5059; Email: jinylee@skku.edu

Dixian Luo − *Laboratory Medicine Center, Huazhong University of Science and Technology Union Shenzhen Hospital (Nanshan Hospital), Shenzhen 518000 Guangdong, China;* orcid.org/0000-0001-6155-8137; Email: luodixian_2@163.com

Quan Liu − *Laboratory Medicine Center, Huazhong University of Science and Technology Union Shenzhen Hospital (Nanshan Hospital), Shenzhen 518000 Guangdong, China*; Email: liu_quan2020@163.com.

Jonathan L. Sessler − *Department of Chemistry, The University of Texas at Austin, Austin, Texas 78712, United States;* orcid.org/0000-0002-9576-1325; Email: sessler@cm.utexas.edu

Jong Seung Kim − *Department of Chemistry, Korea University, Seoul 02841, Korea;* orcid.org/0000-0003-3477-1172; Email: jongskim@korea.ac.kr

Authors

Jusung An − *Department of Chemistry, Korea University, Seoul 02841, Korea*

Kong-Peng Lv − *Laboratory Medicine Center, Huazhong University of Science and Technology Union Shenzhen Hospital (Nanshan Hospital), Shenzhen 518000 Guangdong, China; Department of Interventional Radiology, Shenzhen People's Hospital, (The Second Clinical Medical College, Jinan University; The First Affiliated Hospital, Southern University of Science and Technology), Shenzhen 518020 Guangdong, China;* orcid.org/0000-0001-6270-639X

Calvin V. Chau − *Department of Chemistry, The University of Texas at Austin, Austin, Texas 78712, United States*

Jong Hyeon Lim − *Department of Chemistry, Sungkyunkwan University, Suwon 16419, Korea*

Rakesh Parida − *Department of Chemistry, Sungkyunkwan University, Suwon 16419, Korea*

Xin Huang − *Laboratory Medicine Center, Huazhong University of Science and Technology Union Shenzhen Hospital (Nanshan Hospital), Shenzhen 518000 Guangdong, China*

Snehasish Debnath − *Department of Chemistry, Korea University, Seoul 02841, Korea;* orcid.org/0000-0001-8342-7496

Yunjie Xu − *Department of Chemistry, Korea University, Seoul 02841, Korea*

Siqi Zheng − *Department of Interventional Radiology, Shenzhen People's Hospital, (The Second Clinical Medical College, Jinan University; The First Affiliated Hospital, Southern University of Science and Technology), Shenzhen 518020 Guangdong, China*

Adam C. Sedgwick − *Department of Chemistry, The University of Texas at Austin, Austin, Texas 78712, United States;* orcid.org/0000-0002-3132-2913

Complete contact information is available at: https://pubs.acs.org/10.1021/jacs.4c05978

Author Contributions

#J.A., K.-P.L., C.V.C., and J.H.L. contributed equally to this work. The article was written through contributions of all authors. All authors have given approval to the final version of the article.

Notes

The authors declare no competing financial interest.

ACKNOWLEDGMENTS

This research was supported by the Basic Science Research Program through the National Research Foundation of Korea (NRF) funded by the Ministry of Education (Nos. RS-2023-00273030, J.A., and RS-2023-00241100, Y.X.), the Ministry of Science and ICT, Korea (CRI project no. 2018R1A3B1052702, J.S.K.), and the Technology Innovation Program (or Industrial Strategic Technology Development Program) (20016007, J.Y.L.) funded by the Ministry of Trade, Industry and Energy (MOTIE, Korea). This study was also supported financially by the General Projects of the National Natural Science Foundation of China (Nos. 82273236, D.X.L., and 82272779, Q.L.), the National Science Fund for Distinguished Young Scholars of China (No. 82003036, Q.L., and 41903056, K.P.L.), the Guangdong Basic and Applied Basic Research Foundation (No. 2023A1515030182, Q.L.), the Science and Technology Innovation Commission of Shenzhen (No. JCYJ20220530141608020, Q.L.), and the Shenzhen Nanshan District Science and Technology Project (No. NSZD2023013, Q.L.). The work in Austin was supported by the Robert A. Welch Foundation (F-0018, J.L.S.) and the National Institutes of Health (CA 068682, J.L.S.). We thank Xu-Dong Chen for early help with the synthetic aspects of this project.

REFERENCES

(1) Castano, A. P.; Mroz, P.; Hamblin, M. R. Photodynamic therapy and anti-tumour immunity. *Nat. Rev. Cancer* **2006**, *6*, 535−545.

(2) Agostinis, P.; Berg, K.; Cengel, K. A.; Foster, T. H.; Girotti, A. W.; Gollnick, S. O.; Hahn, S. M.; Hamblin, M. R.; Juzeniene, A.; Kessel, D.; Korbelik, M.; Moan, J.; Mroz, P.; Nowis, D.; Piette, J.; Wilson, B. C.; Golab, J. Photodynamic therapy of cancer: An update. *CA-Cancer J. Clin.* **2011**, *61*, 250−281.

(3) Lu, Y.; Sun, W.; Du, J.; Fan, J.; Peng, X. Immuno-photodynamic Therapy (IPDT): Organic Photosensitizers and Their Application in Cancer Ablation. *JACS Au* **2023**, *3*, 682−699.

(4) Duan, X.; Chan, C.; Guo, N.; Han, W.; Weichselbaum, R. R.; Lin, W. Photodynamic Therapy Mediated by Nontoxic Core−Shell Nanoparticles Synergizes with Immune Checkpoint Blockade To Elicit Antitumor Immunity and Antimetastatic Effect on Breast Cancer. *J. Am. Chem. Soc.* **2016**, *138*, 16686−16695.

(5) Wachowska, M.; Muchowicz, A.; Golab, J. Targeting Epigenetic Processes in Photodynamic Therapy-Induced Anticancer Immunity. *Front. Oncol.* **2015**, *5*, No. 176.

(6) Zhang, M.; Zhao, Y.; Ma, H.; Sun, Y.; Cao, J. How to improve photodynamic therapy-induced antitumor immunity for cancer treatment? *Theranostics* **2022**, *12*, 4629−4655.
(7) Saxena, M.; van der Burg, S. H.; Melief, C. J. M.; Bhardwaj, N. Therapeutic cancer vaccines. *Nat. Rev. Cancer* **2021**, *21*, 360−378.
(8) Yu, L.; Xu, Y.; Pu, Z.; Kang, H.; Li, M.; Sessler, J. L.; Kim, J. S. Photocatalytic Superoxide Radical Generator that Induces Pyroptosis in Cancer Cells. *J. Am. Chem. Soc.* **2022**, *144*, 11326−11337.
(9) Castano, A. P.; Demidova, T. N.; Hamblin, M. R. Mechanisms in photodynamic therapy: part one—photosensitizers, photochemistry and cellular localization. *Photodiagn. Photodyn. Ther.* **2004**, *1*, 279−293.
(10) Wang, Y.-Y.; Liu, Y.-C.; Sun, H.; Guo, D.-S. Type I photodynamic therapy by organic−inorganic hybrid materials: From strategies to applications. *Coord. Chem. Rev.* **2019**, *395*, 46−62.
(11) Swamy, P. C. A.; Sivaraman, G.; Priyanka, R. N.; Raja, S. O.; Ponnuvel, K.; Shanmugpriya, J.; Gulyani, A. Near Infrared (NIR) absorbing dyes as promising photosensitizer for photo dynamic therapy. *Coord. Chem. Rev.* **2020**, *411*, No. 213233.
(12) Xu, Y.; Zhang, Y.; Li, J.; An, J.; Li, C.; Bai, S.; Sharma, A.; Deng, G.; Kim, J. S.; Sun, Y. NIR-II emissive multifunctional AIEgen with single laser-activated synergistic photodynamic/photothermal therapy of cancers and pathogens. *Biomaterials* **2020**, *259*, No. 120315.
(13) Li, M.; Gebremedhin, K. H.; Ma, D.; Pu, Z.; Xiong, T.; Xu, Y.; Kim, J. S.; Peng, X. Conditionally Activatable Photoredox Catalysis in Living Systems. *J. Am. Chem. Soc.* **2022**, *144*, 163−173.
(14) Li, M.; Xu, Y.; Pu, Z.; Xiong, T.; Huang, H.; Long, S.; Son, S.; Yu, L.; Singh, N.; Tong, Y.; Sessler, J. L.; Peng, X.; Kim, J. S. Photoredox catalysis may be a general mechanism in photodynamic therapy. *Proc. Natl. Acad. Sci. U.S.A.* **2022**, *119*, No. e2210504119.
(15) Nguyen, V.-N.; Qi, S.; Kim, S.; Kwon, N.; Kim, G.; Yim, Y.; Park, S.; Yoon, J. An Emerging Molecular Design Approach to Heavy-Atom-Free Photosensitizers for Enhanced Photodynamic Therapy under Hypoxia. *J. Am. Chem. Soc.* **2019**, *141*, 16243−16248.
(16) Nguyen, V.-N.; Yan, Y.; Zhao, J.; Yoon, J. Heavy-Atom-Free Photosensitizers: From Molecular Design to Applications in the Photodynamic Therapy of Cancer. *Acc. Chem. Res.* **2021**, *54*, 207−220.
(17) Zhang, Y.-H.; Li, X.; Huang, L.; Kim, H. S.; An, J.; Lan, M.; Cao, Q.-Y.; Kim, J. S. AIE based GSH activatable photosensitizer for imaging-guided photodynamic therapy. *Chem. Commun.* **2020**, *56*, 10317−10320.
(18) Won, M.; Koo, S.; Li, H.; Sessler, J. L.; Lee, J. Y.; Sharma, A.; Kim, J. S. An Ethacrynic Acid-Brominated BODIPY Photosensitizer (EA-BPS) Construct Enhances the Lethality of Reactive Oxygen Species in Hypoxic Tumor-Targeted Photodynamic Therapy. *Angew. Chem., Int. Ed.* **2021**, *60*, 3196−3204.
(19) Jung, E.; Shim, I.; An, J.; Ji, M. S.; Jangili, P.; Chi, S.-G.; Kim, J. S. Phenylthiourea-Conjugated BODIPY as an Efficient Photosensitizer for Tyrosinase-Positive Melanoma-Targeted Photodynamic Therapy. *ACS Appl. Bio Mater.* **2021**, *4*, 2120−2127.
(20) Han, H.-H.; Wang, H.-M.; Jangili, P.; Li, M.; Wu, L.; Zang, Y.; Sedgwick, A. C.; Li, J.; He, X.-P.; James, T. D.; Kim, J. S. The design of small-molecule prodrugs and activatable phototherapeutics for cancer therapy. *Chem. Soc. Rev.* **2023**, *52*, 879−920.
(21) Jung, H. S.; Han, J.; Shi, H.; Koo, S.; Singh, H.; Kim, H.-J.; Sessler, J. L.; Lee, J. Y.; Kim, J.-H.; Kim, J. S. Overcoming the Limits of Hypoxia in Photodynamic Therapy: A Carbonic Anhydrase IX-Targeted Approach. *J. Am. Chem. Soc.* **2017**, *139*, 7595−7602.
(22) Li, M.; Shao, Y.; Kim, J. H.; Pu, Z.; Zhao, X.; Huang, H.; Xiong, T.; Kang, Y.; Li, G.; Shao, K.; Fan, J.; Foley, J. W.; Kim, J. S.; Peng, X. Unimolecular Photodynamic O_2-Economizer To Overcome Hypoxia Resistance in Phototherapeutics. *J. Am. Chem. Soc.* **2020**, *142*, 5380−5388.
(23) Koo, S.; Lee, M.-G.; Sharma, A.; Li, M.; Zhang, X.; Pu, K.; Chi, S.-G.; Kim, J. S. Harnessing GLUT1-Targeted Pro-oxidant Ascorbate for Synergistic Phototherapeutics. *Angew. Chem., Int. Ed.* **2022**, *61*, No. e202110832.
(24) An, J.; Tang, S.; Hong, G.; Chen, W.; Chen, M.; Song, J.; Li, Z.; Peng, X.; Song, F.; Zheng, W.-H. An unexpected strategy to alleviate hypoxia limitation of photodynamic therapy by biotinylation of photosensitizers. *Nat. Commun.* **2022**, *13*, No. 2225.
(25) Höckel, M.; Vaupel, P. Tumor Hypoxia: Definitions and Current Clinical, Biologic, and Molecular Aspects. *JNCI J. Natl. Cancer Inst.* **2001**, *93*, 266−276.
(26) Preihs, C.; Arambula, J. F.; Magda, D.; Jeong, H.; Yoo, D.; Cheon, J.; Siddik, Z. H.; Sessler, J. L. Recent Developments in Texaphyrin Chemistry and Drug Discovery. *Inorg. Chem.* **2013**, *52*, 12184−12192.
(27) Ren, Y.; Sedgwick, A. C.; Chen, J.; Thiabaud, G.; Chau, C. V.; An, J.; Arambula, J. F.; He, X.-P.; Kim, J. S.; Sessler, J. L.; Liu, C. Manganese(II) Texaphyrin: A Paramagnetic Photoacoustic Contrast Agent Activated by Near-IR Light. *J. Am. Chem. Soc.* **2020**, *142*, 16156−16160.
(28) Young, S. W.; Woodburn, K. W.; Wright, M.; Mody, T. D.; Fan, Q.; Sessler, J. L.; Dow, W. C.; Miller, R. A. Lutetium Texaphyrin (PCI-0123): A Near-Infrared, Water-Soluble Photosensitizer. *Photochem. Photobiol.* **1996**, *63*, 892−897.
(29) Grossweiner, L. I.; Bilgin, M. D.; Berdusis, P.; Mody, T. D. Singlet Oxygen Generation by Metallotexaphyrins. *Photochem. Photobiol.* **1999**, *70*, 138−145.
(30) Blumenkranz, M. S.; Woodburn, K. W.; Qing, F.; Verdooner, S.; Kessel, D.; Miller, R. Lutetium texaphyrin (Lu-Tex): a potential new agent for ocular fundus angiography and photodynamic therapy. *Am. J. Ophthalmol.* **2000**, *129*, 353−362.
(31) Leahy, K. M.; Ornberg, R. L.; Wang, Y.; Zweifel, B. S.; Koki, A. T.; Masferrer, J. L. Cyclooxygenase-2 Inhibition by Celecoxib Reduces Proliferation and Induces Apoptosis in Angiogenic Endothelial Cells in Vivo. *Cancer Res.* **2002**, *62*, 625−631.
(32) Gately, S.; Li, W. W. Multiple roles of COX-2 in tumor angiogenesis: a target for antiangiogenic therapy. *Semin. Oncol.* **2004**, *31*, 2−11.
(33) Ghosh, N.; Chaki, R.; Mandal, V.; Mandal, S. C. COX-2 as a target for cancer chemotherapy. *Pharmacol. Rep.* **2010**, *62*, 233−244.
(34) Masferrer, J. L.; Leahy, K. M.; Koki, A. T.; Zweifel, B. S.; Settle, S. L.; Woerner, B. M.; Edwards, D. A.; Flickinger, A. G.; Moore, R. J.; Seibert, K. Antiangiogenic and Antitumor Activities of Cyclooxygenase-2 Inhibitors. *Cancer Res.* **2000**, *60*, 1306−1311.
(35) Bhuvaneswari, R.; Gan, Y. Y.; Soo, K. C.; Olivo, M. The effect of photodynamic therapy on tumor angiogenesis. *Cell. Mol. Life Sci.* **2009**, *66*, 2275−2283.
(36) Liu, Q.; Fan, T.; Zheng, Y.; Yang, S.-l.; Yu, Z.; Duo, Y.; Zhang, Y.; Adah, D.; Shi, L.; Sun, Z.; Wang, D.; Xie, J.; Wu, H.; Wu, Z.; Ge, C.; Qiao, L.; Wei, C.; Huang, L.; Yan, Q.; Yang, Q.; Bao, S.; Liu, L.-P.; Zhang, H. Immunogenic exosome-encapsulated black phosphorus nanoparticles as an effective anticancer photo-nanovaccine. *Nanoscale* **2020**, *12*, 19939−19952.
(37) Sun, Z.; Fan, T.; Liu, Q.; Huang, L.; Hu, W.; Shi, L.; Wu, Z.; Yang, Q.; Liu, L.; Zhang, H. Autologous tumor antigens and boron nanosheet-based nanovaccines for enhanced photo-immunotherapy against immune desert tumors. *Nanophotonics* **2021**, *10*, 2519−2535.
(38) Liu, Q.; Duo, Y.; Fu, J.; Qiu, M.; Sun, Z.; Adah, D.; Kang, J.; Xie, Z.; Fan, T.; Bao, S.; Zhang, H.; Liu, L.-P.; Cao, Y. Nano-immunotherapy: Unique mechanisms of nanomaterials in synergizing cancer immunotherapy. *Nano Today* **2021**, *36*, No. 101023.
(39) Xie, Z.; Fan, T.; An, J.; Choi, W.; Duo, Y.; Ge, Y.; Zhang, B.; Nie, G.; Xie, N.; Zheng, T.; Chen, Y.; Zhang, H.; Kim, J. S. Emerging combination strategies with phototherapy in cancer nanomedicine. *Chem. Soc. Rev.* **2020**, *49*, 8065−8087.
(40) Jang, J.-W.; Song, Y.; Kim, S.-H.; Kim, J.; Seo, H. R. Potential mechanisms of CD133 in cancer stem cells. *Life Sci.* **2017**, *184*, 25−29.
(41) Sessler, J. L.; Mody, T. D.; Hemmi, G. W.; Lynch, V. Synthesis and structural characterization of lanthanide(III) texaphyrins. *Inorg. Chem.* **1993**, *32*, 3175−3187.

https://doi.org/10.1021/jacs.4c05978
J. Am. Chem. Soc. XXXX, XXX, XXX−XXX

(42) Lammer, A. D.; Thiabaud, G.; Brewster, J. T., II; Alaniz, J.; Bender, J. A.; Sessler, J. L. Lanthanide Texaphyrins as Photocatalysts. *Inorg. Chem.* **2018**, *57*, 3458−3464.
(43) Gurram, B.; Zhang, S.; Li, M.; Li, H.; Xie, Y.; Cui, H.; Du, J.; Fan, J.; Wang, J.; Peng, X. Celecoxib Conjugated Fluorescent Probe for Identification and Discrimination of Cyclooxygenase-2 Enzyme in Cancer Cells. *Anal. Chem.* **2018**, *90*, 5187−5193.
(44) Wang, B.; Fan, J.; Wang, X.; Zhu, H.; Wang, J.; Mu, H.; Peng, X. A Nile blue based infrared fluorescent probe: imaging tumors that over-express cyclooxygenase-2. *Chem. Commun.* **2015**, *51*, 792−795.
(45) Zhang, H.; Fan, J.; Wang, J.; Dou, B.; Zhou, F.; Cao, J.; Qu, J.; Cao, Z.; Zhao, W.; Peng, X. Fluorescence Discrimination of Cancer from Inflammation by Molecular Response to COX-2 Enzymes. *J. Am. Chem. Soc.* **2013**, *135*, 17469−17475.
(46) Wilkinson, F.; Helman, W. P.; Ross, A. B. Quantum Yields for the Photosensitized Formation of the Lowest Electronically Excited Singlet State of Molecular Oxygen in Solution. *J. Phys. Chem. Ref. Data* **1993**, *22*, 113−262.
(47) Catalán, J. Toward a Generalized Treatment of the Solvent Effect Based on Four Empirical Scales: Dipolarity (SdP, a New Scale), Polarizability (SP), Acidity (SA), and Basicity (SB) of the Medium. *J. Phys. Chem. B* **2009**, *113*, 5951−5960.
(48) Coutsias, E. A.; Seok, C.; Dill, K. A. Using quaternions to calculate RMSD. *J. Comput. Chem.* **2004**, *25*, 1849−1857.
(49) Chatterjee, S.; Salimi, A.; Lee, J. Y. Insights into amyotrophic lateral sclerosis linked Pro525Arg mutation in the fused in sarcoma protein through in silico analysis and molecular dynamics simulation. *J. Biomol. Struct. Dyn.* **2021**, *39*, 5963−5976.
(50) Chen, Y.-L.; Li, S.-W.; Chi, Y.; Cheng, Y.-M.; Pu, S.-C.; Yeh, Y.-S.; Chou, P.-T. Switching Luminescent Properties in Osmium-Based *β*-Diketonate Complexes. *ChemPhysChem* **2005**, *6*, 2012−2017.
(51) Fujii, M.; Kovalev, D.; Goller, B.; Minobe, S.; Hayashi, S.; Timoshenko, V. Y. Time-resolved photoluminescence studies of the energy transfer from excitons confined in Si nanocrystals to oxygen molecules. *Phys. Rev. B* **2005**, *72*, No. 165321.
(52) Seybold, P. G.; Gouterman, M.; Callis, J. Calorimetric, Photometric and Lifetime Determinations of Fluorescence Yields of Fluorescein Dyes. *Photochem. Photobiol.* **1969**, *9*, 229−242.
(53) Mongelard, F.; Bouvet, P. AS-1411, a guanosine-rich oligonucleotide aptamer targeting nucleolin for the potential treatment of cancer, including acute myeloid leukemia. *Curr. Opin. Mol. Ther.* **2010**, *12*, 107−114.
(54) Alibolandi, M.; Abnous, K.; Anvari, S.; Mohammadi, M.; Ramezani, M.; Taghdisi, S. M. CD133-targeted delivery of self-assembled PEGylated carboxymethylcellulose-SN38 nanoparticles to colorectal cancer. *Artif. Cells, Nanomed., Biotechnol.* **2018**, *46*, 1159−1169.

https://doi.org/10.1021/jacs.4c05978
J. Am. Chem. Soc. XXXX, XXX, XXX−XXX